PHYSICAL REVIEW B **82**, 075432 (2010)

Multiferroic $BiFeO_3$-$BiMnO_3$ nanoscale checkerboard from first principles

L. Pálová, P. Chandra, and K. M. Rabe
Center for Materials Theory, Department of Physics and Astronomy, Rutgers University, Piscataway, New Jersey 08854, USA
(Received 24 June 2010; published 31 August 2010)

We present a first principles study of an unusual heterostructure, an atomic-scale checkerboard of $BiFeO_3$-$BiMnO_3$, and compare its properties to the two bulk constituent materials, $BiFeO_3$ and $BiMnO_3$. The "nanocheckerboard" is found to have a multiferroic ground state with the desired properties of each constituent: polar and ferrimagnetic due to $BiFeO_3$ and $BiMnO_3$, respectively. The effect of B-site cation ordering on magnetic ordering in the $BiFeO_3$-$BiMnO_3$ system is studied. The checkerboard geometry is seen to give rise to a magnetostructural effect that is neither present in the bulk constituent materials, nor in the layered $BiFeO_3$-$BiMnO_3$ superlattice.

DOI: 10.1103/PhysRevB.82.075432 PACS number(s): 75.80.+q, 75.75.−c, 77.80.−e

I. INTRODUCTION

Artificially structured oxides present intriguing opportunities for material design. With dramatic advances in epitaxial growth techniques allowing atomic-scale control, experimental and theoretical attention has focused on strained-layer superlattices.[1–10] Properties significantly different from those in the bulk have been observed, leading to the possibility of designing new materials at the nanoscale with enhanced functionalities.[11–13] Recently, progress has been reported in the synthesis of artificially structured oxides with lateral "nanocheckerboard" (or nanopillar) patterning. In particular, the length scale of this checkerboard ordering can be controlled by synthetic processes and stoichiometry, offering promise for applications such as ultra-high-density magnetic recording media.[14–19]

One functionality of particular current interest is multiferroicity: the combination of ferromagnetism and ferroelectricity, with coupling between the spontaneous polarization and the magnetization. Room-temperature multiferroic materials with high magnetoelectric couplings are desirable, because they can support novel functionalities in electronic devices.[20,21] Magnetostructural and magnetoelectric couplings have been observed in a number of materials, including bulk[22,23] and layered[24] manganites, epitaxial $EuTiO_3$,[25] $EuSe/PbSe_{1-x}Te_x$ multilayers,[26] and $SrRuO_3/SrTiO_3$ oxide interfaces.[27]

Because of the distinct natures of ferroelectric and ferromagnetic ordering, it has proved difficult to find a single-phase room-temperature multiferroic material with large polarization, large magnetization, and large magnetoelectric and/or magnetoelastic coupling.[28] Most current multiferroic devices are based on nanocomposites,[21,29] and advances in the synthesis of artificially structured materials further support studies of novel multiferroic heterostructures.[30] Exploring the coupling of ferroelectric and/or magnetic states to strain has shown to be exceptionally fruitful in many multiferroic nanocomposites.[29] The challenge is to anticipate what new properties can arise in such heterostructures from combining two distinct materials, and how these properties depend on the geometry of the combination.

First-principles approaches are ideally suited for meeting this challenge. These methods allow searching over a variety of compositions, heterostructure geometries, and structure types to find a material with the desired properties.[31] With first-principles methods, it is possible also to identify and characterize low-energy alternative structures; though they are not manifest in the bulk, they can become physically relevant with changes in the external parameters and boundary conditions produced in a nanocomposite.

In this paper, we use first principles calculations to explore the structure and properties of a prototypical atomic-scale checkerboard of $BiFeO_3$ and $BiMnO_3$ (Fig. 1), extending a shorter study of this nanocomposite that has been published elsewhere.[32] Ferroelectric antiferromagnetic (AFM) bulk $BiFeO_3$ and half-metallic ferromagnetic (FM) bulk $BiMnO_3$ are good candidates for a nanocomposite with ferroelectric-ferromagnetic (multiferroic) behavior. The properties of the atomic-scale checkerboard are found to be directly related to the properties of the bulk constituents in their ground states and in low-energy alternative structures. The ground state of the $BiFeO_3$-$BiMnO_3$ atomic-scale checkerboard is multiferroic, i.e., ferroelectric and ferrimagnetic, acquiring the desired properties from the constituents. In addition, we show that the $BiFeO_3$-$BiMnO_3$ atomic-scale checkerboard displays a magnetostructural effect, namely, it changes its magnetic ordering with the change of its crystal structure. This effect is argued to be inherent to B-site cation checkerboard geometry, resulting from magnetic frustration for the particular arrangement of cations and bonds.

The organization of this paper follows. In Sec. II, we describe the first-principles method and the structural distortions and magnetic orderings considered. Results for low-energy alternative structures of bulk $BiFeO_3$ and $BiMnO_3$ are reported in Secs. III and IV, respectively. The ground state of the $BiFeO_3$-$BiMnO_3$ atomic-scale checkerboard is shown to be ferroelectric and ferrimagnetic in Sec. V A simple Heisenberg model is constructured to represent the energies of various magnetic states of this checkerboard computed from first principles. In Sec. VI, the effect of structural distortions on the magnetic ordering of the nanocheckerboard is explored, and we relate the properties of alternative low-energy structures of the checkerboard to those of bulk $BiFeO_3$ and $BiMnO_3$. Anisotropic epitaxial strain is shown to drive a magnetic transition in the atomic-scale checkerboard in Sec. VII. We study the effect of B-site cation arrangement on

 ©2010 The American Physical Society

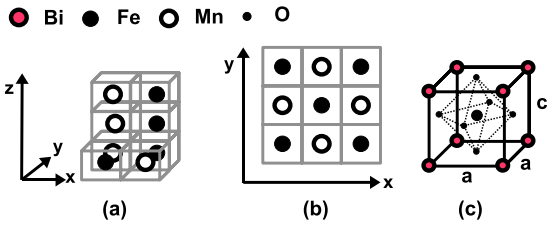

FIG. 1. (Color online) (a) $BiFeO_3$-$BiMnO_3$ atomic-scale checkerboard. (b) Top view of the atomic-scale checkerboard. (c) Perovskite cell. Dashed lines show an oxygen octahedron surrounding the B-site (Fe, or Mn) cation.

magnetic properties of the $BiFeO_3$-$BiMnO_3$ system in Sec. VIII. The possibility of experimentally realizing a $BiFeO_3$-$BiMnO_3$ nanocheckerboard is discussed in Sec. IX. Conclusions are presented in Sec. X.

II. METHOD

First-principles calculations are performed using density functional theory within the local spin-density approximation with Hubbard U (LSDA+U) method as implemented in the Vienna *ab initio* simulation package VASP-4.6.34.[33,34] Projector-augmented wave potentials (PAW)[35,36] are used with 15 valence electrons for Bi($5d^{10}6s^26p^3$), 14 for Fe($3p^63d^64s^2$), 13 for Mn($3p^63d^54s^2$), and 6 for O($2s^22p^4$). The robustness of the results is tested with two different implementations of the rotationally invariant LSDA+U version. The first is due to Liechtenstein[37] with effective on-site Coulomb interaction $U_{Fe}=U_{Mn}=5$ eV and effective on-site exchange interaction $J_{Fe}=J_{Mn}=1$ eV. The second is due to Dudarev,[38] with $U^{eff}_{Mn}=5.2$ eV, $U^{eff}_{Fe}=4$ eV, where $U^{eff}=U-J$. Both implementations treat localized d electron states in Fe and Mn. It has previously been shown that these U and J values give good agreement with experiment in bulk $BiFeO_3$.[39] The value $U^{eff}_{Mn}=5.2$ eV has previously been used for bulk $BiMnO_3$ ground state calculations.[40]

The $BiFeO_3$-$BiMnO_3$ atomic-scale checkerboard is shown in Fig. 1. $BiFeO_3$ and $BiMnO_3$ alternate at the atomic level, forming a checkerboard pattern in the xy plane and pillars of the same composition along z. The supercell is $\sqrt{2}a\times\sqrt{2}a\times 2c$, containing two Fe and two Mn. In the limit of the atomic-scale pillars considered here, the checkerboard structure is the same as that of a (110)-oriented superlattice.

We consider two additional types of B-site cation-ordered $BiFeO_3$-$BiMnO_3$ systems: a (001)-oriented layered superlattice, with single unit-cell Fe and Mn layers alternating along z, and a rocksalt structure, with Fe and Mn alternating in every other unit cell [(111) superlattice in the atomic-scale limit considered here]. In both cases, the supercell is $\sqrt{2}a\times\sqrt{2}a\times 2c$. For consistency, we take the supercell for bulk $BiFeO_3$ and bulk $BiMnO_3$ calculations to be $\sqrt{2}a\times\sqrt{2}a\times 2c$, except for the R3c structure, where we use a $\sqrt{2}a\times\sqrt{2}a\times\sqrt{2}a$ supercell.

Several types of magnetic orderings are studied here: the G-type (rocksalt), C-type, A-type AFM, and FM ordering of the local magnetic moments in bulk $BiFeO_3$, or bulk $BiMnO_3$ (see Fig. 2). All orderings considered are collinear; this is supported by recent neutron scattering measurements on $BiFeO_3$ doped with Mn,[41] that indicate collinear AFM ordering.

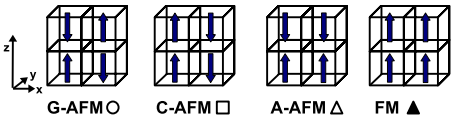

FIG. 2. (Color online) Magnetic orderings considered for bulk $BiFeO_3$ and bulk $BiMnO_3$: Symbols for each type of ordering are introduced next to each label.

Magnetic orderings of the $BiFeO_3$-$BiMnO_3$ atomic-scale checkerboard are shown in Fig. 3, where we consider six collinear orderings of Fe and Mn spins. Similarly, six collinear orderings of the magnetic Fe and Mn spins are explored in the $BiFeO_3$-$BiMnO_3$ (001)-oriented superlattice and the rocksalt structure. For the (001)-oriented superlattice, these orderings are described by the notation FeFM (FeAFM), or MnFM (MnAFM), referring to the FM (AFM) ordering for the Fe (Mn) moments in the relevant layer, respectively, with the remaining ambiguities resolved as follows: FeAFM-MnAFM magnetic order has AFM ordered Fe and Mn layers with FM order along the mixed Fe-Mn chains in the z direction, while G-AFM designates the case with AFM order along the mixed chains; similarly, FeFMMnFM has FM ordered Fe and Mn layers with AFM order, while FM designates the case with FM order along the mixed chains. For the rocksalt structure, we consider FM and G-AFM ordering, FeAFMMnFM ordering, referring to FM ordered Mn sublattice and AFM ordered Fe sublattice; similarly we consider FeFMMnAFM ordering with FM ordered Fe and AFM ordered Mn sublattices, respectively. Finally, the FMFM ordering has AFM ordered Mn and Fe sublattices, which are coupled FM in each Fe-Mn z layer, while the AFMAFM ordering has AFM ordered Mn and Fe sublattices coupled AFM in each Fe-Mn z layer.

Structures generated by three modes of the cubic perovskite structure are considered (see Fig. 4):[44] (i) the zone center polar Γ_4^- mode, (ii) the M_3^+ oxygen octahedron rotations

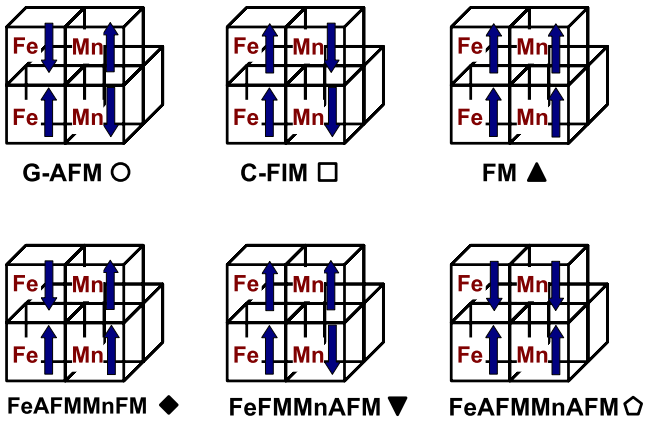

FIG. 3. (Color online) Magnetic orderings considered for the $BiFeO_3$-$BiMnO_3$ atomic-scale checkerboard compatible with the $\sqrt{2}a\times\sqrt{2}a\times 2c$ supercell. Symbols for each type of ordering are introduced next to each label.

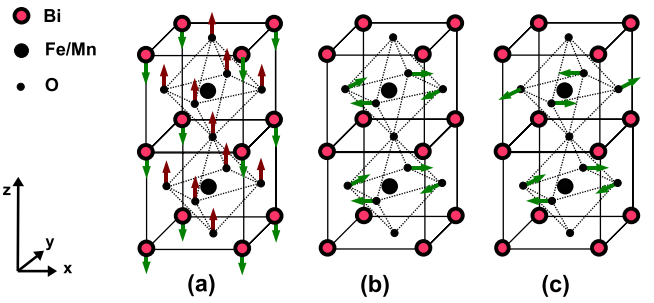

FIG. 4. (Color online) Distortions of the ideal cubic perovskite cell considered in this work (Ref. 44): (a) Polar distortion with relative shift of Bi and Fe/Mn cations with respect to O anions along the z axis ($\Gamma_4^-(z)$), (b) + (in-phase) rotations of the oxygen octahedra (dashed lines)about the z axis [$M_3^+(z)$], (c) − (out-of-phase) rotations of the oxygen octahedra (dashed lines) about the z axis [$R_4^+(z)$].

(all rotations about a given axis are in phase), and (iii) R_4^+ rotations (sense of rotations alternates along the rotation axis). Space groups corresponding to the structural distortions considered are presented in Table I, and we use the notation c-, l-, or r-to refer to the structural distortion of the B-site cation-ordered checkerboard, layered superlattice, or rocksalt structure, respectively. To search for the ground state for a given magnetic ordering and structure type, we perform structural relaxation with the conjugate gradient algorithm. Both the cell shape and the cell volume are relaxed; more specifically, the ions are relaxed toward equilibrium positions until the Hellmann-Feynman forces are less than 10^{-3} eV/Å. An energy cutoff 550 eV for the plane wave basis set is used. Convergence in the energy is reached with precision 10^{-7} eV. A Monkhorst-Pack k-point grid[42] is generated with density $4\times4\times4$ for the $(\sqrt{2}\times\sqrt{2}\times\sqrt{2})$ supercell, and $4\times4\times2$ for the $(\sqrt{2}\times\sqrt{2}\times2)$ supercell. For magnetic energy calculations (Secs. V B and VIII), we use the energy cutoff 800 eV, and the Monkhorst-Pack k-point grid with density $6\times6\times4$. Gaussian broadening of the partial occupancies for each wave function is 0.05 eV. A tetrahedron method with Blochl corrections[43] is used for the density of states (DOS) calculations, with the Monkhorst-Pack k-point grid $4\times4\times4$ for the $(\sqrt{2}\times\sqrt{2}\times\sqrt{2})$ and $8\times8\times4$ for the $(\sqrt{2}\times\sqrt{2}\times2)$ supercell.

The rotational distortion can be quantified using the oxygen octahedron rotational angle Θ defined specifically for each oxygen in the octahedron as

$$\cos\Theta = \frac{\vec{u}\cdot\vec{v}}{|\vec{u}||\vec{v}|}, \tag{1}$$

where $\vec{u}$ is the shortest vector from the rotation axis to the reference position of the oxygen, and $\vec{v}$ is the shortest vector from the rotation axis to the position of the oxygen in the distorted structure. The rotation axis is [001] and [010] for the $M_3^+(z)$ and $R_4^+(y)$ distortions, respectively, and the three-fold axis (body diagonal of the cube or distorted cube) for the $R_4^+([111])$ distortion. Due to deformation of the oxygen octahedron in the $BiFeO_3$-$BiMnO_3$ checkerboard structures, these angles may be different for different oxygens in the same octahedron. We report an average value if the range is small; otherwise the lower and upper limits of the range are presented.

The polar distortions of the various structures can be quantified by estimating the polarization based on a linearized expression with nominal charges:

$$\vec{P} = \frac{|e|}{\Omega}\sum_j q_j \Delta\vec{u}_j, \tag{2}$$

where $\vec{P}$ is the polarization, $\Delta\vec{u}_j$ is the displacement of the jth ion with respect to its ideal perovskite position, q_j is the nominal charge of the jth ion ($q_{Bi}=+3$, $q_{Fe}=+3$, $q_{Mn}=+3$, $q_O=-2$), and Ω is the unit cell volume.

For selected structures the true value for the spontaneous polarization is computed using the Berry phase method[45,46] as implemented in VASP–4.6.34. In this formalism, the polarization is only well-defined *mod* $e\vec{R}/\Omega$, where $\vec{R}$ is any lattice vector and Ω is the primitive-cell volume; thus, possible values of the polarization are points on the lattice defined by $\vec{P}_0+e\vec{R}/\Omega$, where $\vec{P}_0$ is the value directly obtained from the Berry phase calculation. Choosing the lattice point (or ?branch?) that corresponds to the measured switching polarization (e.g., in an electrical hysteresis loop) is done by computing the polarization of states closely spaced along an adiabatic path connecting the structure of interest to a high-symmetry reference structure. These laborious calculations can be avoided by an approach based on the reformulation of the polarization in terms of Wannier function centers;[45] the switching polarization is obtained from the difference between the two symmetry-related variants by associating the Wannier centers with the same atoms in both structures.[47,48] Due to incompatibility between the Wannier90 and the VASP codes, we cannot use this latter approach here; we make the necessary branch choices based on computations along adiabatic paths combined with the nominal-charge polarization estimate.

III. $BiFeO_3$ STRUCTURES

In agreement with previous first-principles calculations and experiment,[39,41,49,50] we find that the ground state structure of $BiFeO_3$ has rhombohedral R3c symmetry, which is a combination of the rotational $R_4^+([111])$ mode (counter-

TABLE I. Resulting space groups for considered structural distortions (see Fig. 4). $Pm\bar{3}m$ is the ideal perovskite structure and P4/mmm is the uniformly strained tetragonal unit cell.

Modes	$\Gamma_4^-(z)$	$M_3^+(z)$	$M_3^+(z)$, $\Gamma_4^-(z)$	$R_4^+(y)$	$R_4^+(y)$, $\Gamma_4^-(y)$	$R_4^+([111])$	$R_4^+([111])$, $\Gamma_4^-([111])$
Abbrevation	$\Gamma_4^-(z)$	$M_3^+(z)$	$M\Gamma(z)$	$R_4^+(y)$	$R\Gamma(y)$	$R_4^+(d)$	$R\Gamma(d)$
Space Group	P4mm	P4/mbm	P4bm	I4/mcm	I4cm	$R\bar{3}c$	R3c

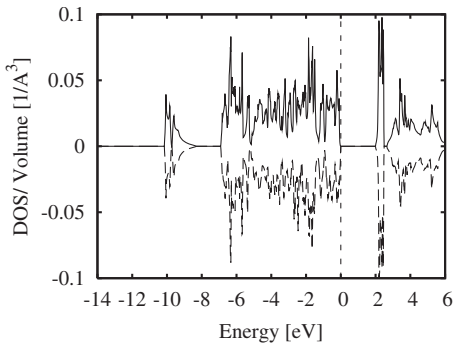

FIG. 5. Density of states (DOS) of the R3c G-AFM ground state (GS) of $BiFeO_3$. Spin up states are plotted by solid line and spin down states by a dashed line (inverted view). The zero is set to the valence band maximum. DOS shows an insulating band gap of 2 eV.

rotations of the oxygen octahedra about the [111] axis) and a polar $\Gamma_4^-([111])$ modes, with Bi, Fe, and O displaced relative to one another along [111] and further distortion of the oxygen octahedra by displacement of the O displaced perpendicular to [111].[44] The oxygen octahedra rotation angle is large, about 14°, and is comparable to rotations in other perovskites.[51] The R3c ground state has G-AFM (rocksalt) ordering (see Fig. 2), and Fe local magnetic moment of $4\mu_B$.[41] The density of states (DOS) is plotted in Fig. 5: it has a 2 eV band gap that separates occupied and unoccupied Fe *d* states. The polar character of $BiFeO_3$ arises from the polar $\Gamma_4^-([111])$ mode, and the spontaneous polarization using the Berry phase method is $P^{R3c}=90\ \mu C/cm^2$ along the [111] direction.

Next alternative structures of $BiFeO_3$ are studied, and we consider those generated by freezing in linear combinations of the rotational M_3^+, R_4^+, and polar Γ_4^- modes, and four magnetic orderings (see Fig. 2). Their energies are plotted in Fig. 6 (see also Table II). By symmetry, the FM ordering has the same energy for the $\Gamma_4^-(z)$ and $\Gamma_4^-(y)$ structures; this is also true for the G-AFM ordering. In contrast, the C-AFM ordering has different energy for the $\Gamma_4^-(z)$ and $\Gamma_4^-(y)$ structures; this is also true for the A-AFM ordering, as the y and z

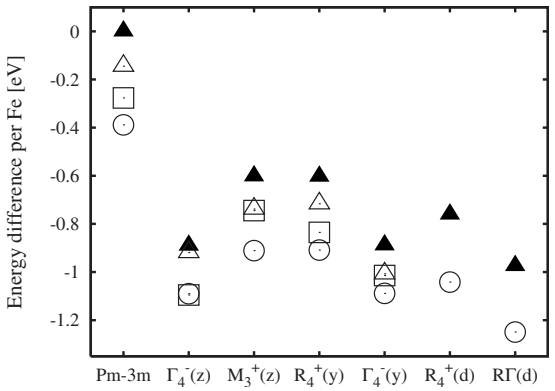

FIG. 6. Structural energetics of bulk $BiFeO_3$. Energy difference per Fe for different magnetic orderings (see Fig. 2) and structural distortions (see Fig. 4 and Table I) relative to the FM $Pm\bar{3}m$ structure.

TABLE II. GS and low-energy alternative structures of bulk $BiFeO_3$. The energy difference ΔE is given with respect to the FM $Pm\bar{3}m$ structure, as in Fig. 6. Polarization *P* is estimated from the nominal charges [Eq. (2)]. Also included are the band gap Δ and the a and c lattice constants for the $\sqrt{2}a\times\sqrt{2}a\times 2c$ supercell of P4mm, and the a lattice constant and the angle α for the $\sqrt{2}a\times\sqrt{2}a\times\sqrt{2}a$ supercell of R3c.

Space group	P4mm		R3c
Modes	$\Gamma_4^-(z)$		$R_4^+([111])$, $\Gamma_4^-([111])$
Mag. order	G-AFM	C-AFM	G-AFM
ΔE [ev/Fe]	−1.09	−1.10	−1.25
Δ [eV]	1.75	2.23	1.99
P[$\mu C/cm^2$]	113.6	116.2	62.1
a/c [Å]	3.68/4.64	3.67/4.68	5.52, α=59.8°

directions for these spin arrangements are not symmetry-related (see Figs. 2 and 6).

For all structural distortions considered, the favored magnetic ordering is G-AFM (open circle). This is consistent with the Goodenough-Kanamori rules: either a strong σ bond is formed between Fe e_g and the neighboring O *p* orbitals in an ideal 180° Fe-O-Fe bond (ideal perovskite structure), or a weak π bond is formed between Fe t_{2g} and O *p* orbitals when the bond is bent toward 90° (as the structure is distorted); in both cases, the AFM superexchange is favored.[52–54]

The most favorable low-energy alternative structures and the ground state of $BiFeO_3$ are presented in Table II. The low-energy $\Gamma_4^-(z)$ structure, with P4mm symmetry, is the supertetragonal structure with $c/a\sim 1.3$, previously discussed elsewhere.[55,56] It has been shown recently that this phase can be stabilized in $BiFeO_3$ thin films.[57] The polarization computed by the Berry phase method[55] is $P^{P4mm}\approx 150\ \mu C/cm^2$. The nominal-charge estimates are therefore smaller than the true values for both the P4mm and R3c structures, but the relative values are well reproduced. The polar distortion is dominant in all structures considered; the rotation-only structures are higher in energy, and the pres-

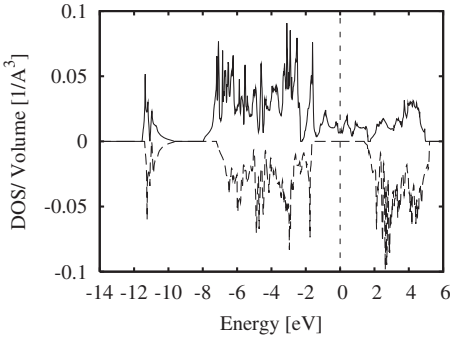

FIG. 7. Density of states (DOS) of the R3c FM alternative structure of $BiMnO_3$. Spin up states are plotted by solid line and spin down states by a dashed line (inverted view). Fermi energy is shown by the vertical dashed line crossing zero. DOS shows a half-metallic character.

TABLE III. Low-energy alternative structures of FM bulk $BiMnO_3$. The energy difference ΔE is calculated with respect to the G-AFM $Pm\bar{3}m$ structure (as in Fig. 8). Listed are values of the spin-down band gap Δ_{hm} in the half-metallic structures or metallic (m) character, the oxygen octahedron rotational angle Θ (see Sec. II), and the a and c lattice constants of the $\sqrt{2}\times\sqrt{2}\times 2$ supercell.

Space group	P4/mmmm	P4bm	I4cm	R3c
Modes		$M_3^+(z)$, $\Gamma_4^-(z)$	$R_4^+(y)$, $\Gamma_4^-(y)$	$R_4^+([111])$, $\Gamma_4^-([111])$
ΔE [eV/Mn]	−0.57	−1.02	−1.03	−1.22
Δ_{hm} [eV]	m	0.73	2.74	3.25
Θ[°]		11.4	12.0	13.3
a/c [Å]	3.83/3.86	3.81/4.01	3.81/3.83	5.51, α=60°

ence of a polar distortion tends to stabilize the rotational instabilities. For example, the $\Gamma_4^-+M_3^+$ and $\Gamma_4^-+R_4^+$ distortions relax back to Γ_4^- with zero oxygen octahedron rotation angle. The only exception is the R3c structure, in which the rotational and polar distortions coexist.

IV. $BIMNO_3$ STRUCTURES

Previous first principles calculations show that the ground state structure of bulk $BiMnO_3$ is monoclinic centrosymmetric C2/c with zero spontaneous polarization[40] and FM ordering.[58–60] Bismuth (Bi) cations are off-center due to stereochemically active Bi lone pairs, and the Jahn-Teller activity of Mn^{3+} further distorts the structure.[61] Optimizing the atomic positions and lattice constants, we performed a first-principles calculation for this structure to find an energy gain of 1.26 eV/Mn relative to the ideal cubic perovskite structure with G-AFM ordering and a_0=3.83 Å; the latter is used as our reference state throughout this section.

We study low-energy alternative structures of $BiMnO_3$ compatible with a $\sqrt{2}\times\sqrt{2}\times 2$ supercell. Results are presented in Fig. 8. The lowest energy structure has R3c symmetry, the same structure type as the ground state of $BiFeO_3$. It is FM, with magnetic moment $3.9\mu_B$ per Mn. This structure lies only 43 meV/Mn above the $BiMnO_3$ monoclinic ground state. The computed DOS is shown in Fig. 7: the system is half-metallic, with a gap of 3.25 eV in the spin down channel. As an aside, we note that it might be useful to stabilize $BiMnO_3$ as a half-metal in this low-energy structure for possible applications in spintronics.[62]

For all structural distortions considered, the favored magnetic ordering is FM, consistent with previous analysis that showed that $BiMnO_3$ favors FM structures with a half-metallic character.[61,63] The ferromagnetism in $BiMnO_3$ can be explained by a combination of Goodenough-Kanamori rules and orbital ordering.[28,59,61,64] Structural distortions (either oxygen octahedron rotations or polar distortion) widen the spin-down gap (see Table III); a similar trend is observed for the band gap in $BiFeO_3$ (see Table II). A small band gap opens with a monoclinic distortion in the FM $BiMnO_3$ ground state.[60,61]

The Jahn-Teller active Mn^{3+} configuration tends to favor elongation of the oxygen octahedron. In contrast to $BiFeO_3$, in which the polar instability strongly dominates, the rotational and polar instabilities in $BiMnO_3$ are comparable in magnitude, as can be seen by comparing the energies of the $\Gamma_4^-(z)$, $M_3^+(z)$ and $R_4^+(y)$ states. The latter two states have a small residual polar instability. A polar distortion along a Cartesian axis lowers the energy of the G-AFM state so that the energy difference between this state and the FM ground state is greatly reduced; this does not occur if the polar distortion is along [111] as in the R3c phase. The octahedral rotation angles in the low-energy $BiMnO_3$ structures are all similar in magnitude, varying between 11–14°, with an angle of 13° for the FM R3c structure. The value of the octahedral rotation angle in the G-AFM R3c structure, 14°, is the same as in G-AFM R3c $BiFeO_3$.

V. $BIFEO_3$-$BIMNO_3$ NANOCHECKERBOARD GROUND STATE

A. Crystal structure, magnetization, and polarization

In the search for the ground state of the atomic-scale checkerboard cation ordering, we considered the six collinear magnetic states of Fig. 3 and four different structures: the tetragonal P4/mmm structure and three additional structures, obtained by freezing in a Γ_4^-(z) mode, a combination of R_4^+(y) and Γ_4^-(y), and a combination of R_4^+(111) and Γ_4^-(111). We designate these latter three structures by the space group they would have if all B sites were occupied by the same cation, with the prefix c to remind us that the actual symmetry is lower due to the checkerboard ordering: c-P4mm, c-I4cm, and c-R3c. The GS of the $BiFeO_3$-$BiMnO_3$ nanocheckerboard is found to be c-R3c, as could be expected based on the R3c GS of bulk $BiFeO_3$, and on our results for bulk $BiMnO_3$. The magnetic ordering in the c-R3c GS is FeAFMMnFM. Fe magnetic moments are ordered AFM along the Fe pillars and Mn magnetic moments are ordered FM along the Mn pillars, as expected from the G-AFM and FM ground states of $BiFeO_3$ and $BiMnO_3$, respectively (see Secs. III and IV). AFM and FM xy layers alternate along z as is sketched in Fig. 3. The computed Fe and Mn local magnetic moments are $4.1\mu_B$ and $3.8\mu_B$, respectively; these are the same values as those reported here in the parent compounds $BiFeO_3$ and $BiMnO_3$. Although the contribution from Fe magnetic moments to the net magnetization

cancels due to the AFM pillar ordering, the contribution from Mn moments adds, leading to a net magnetization of $3.8\mu_B$ per Fe-Mn pair.

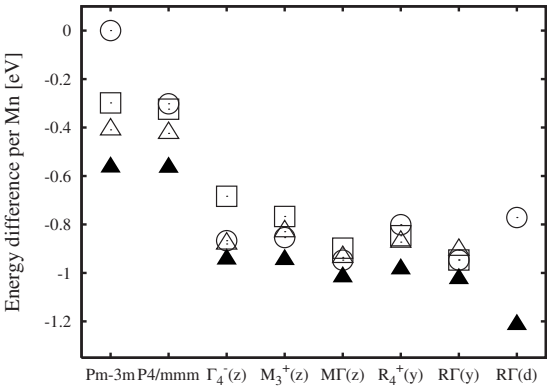

FIG. 8. Structural energetics of bulk $BiMnO_3$. Energy difference per perovskite cell (Mn) for different magnetic orderings (see Fig. 2) and for structural distortions (see Fig. 4 and Table I) generated by the specified modes.

The DOS of the c-R3c FeAFMMnFM GS is shown in Fig. 9. The general features are very similar to those found in $BiFeO_3$ (Fig. 5) and $BiMnO_3$ (Fig. 7), the main difference being that the spin-up Mn states at the Fermi level in $BiMnO_3$ have split to open a gap, with the occupied states at the top of the valence band narrowing the gap to 0.9 eV.

Direct calculation of the spontaneous polarization using the Berry phase method for the c-R3c GS yields a value of $\vec{P}=(19.6,-1.1,30.5)\ \mu C/cm^2$. This is well defined only up to the polarization lattice $e\vec{R}/\Omega$,[45,46] which in this case is $(13.2,13.1,0.1)n_1+(-13.2,13.0,0.1)n_2$ $+(0.0,0.2,26.6)n_3\ \mu C/cm^2$, where $\vec{n}$ is a vector of integers. To determine the branch that corresponds to the switching polarization, we compute the polarization along a structural deformation path that linearly connects the c-R3c GS to the ideal cubic perovskite structure. As shown in Fig. 10, the computation is performed for structures down to 75% of the full distortion (at which point the structures become metallic) and then linearly extrapolated to 0% using the expression

$$\Delta\vec{P}_{100\%-0\%}=4\times\Delta\vec{P}_{100\%-75\%}=(33.8,33.5,39.8)\ \mu C/cm^2. \quad (3)$$

The magnitude of this estimate, 62.0 $\mu C/cm^2$, suggests the branch choice $\vec{P}_{bp}=(32.9,38.0,30.7)\ \mu C/cm^2$ with magnitude $|P_{bp}|=58.9\ \mu C/cm^2$. However, we would expect it to be considerably larger, based on comparison between the Berry phase $|P|$ of bulk $BiFeO_3$ and the $|P|$ computed using nominal charges (see Sec. III); following this intuition we would make the branch choice $\vec{P}_{bp}=(46.1,51.3,57.4)\ \mu C/cm^2$ with magnitude $|P_{bp}|=89.7\ \mu C/cm^2$. This remaining ambiguity highlights the challenge of picking the right branch when the polarization is much larger than the quantum; in either case it is clear that the polarization of the checkerboard is comparable to the largest values found in ferroelectrics. Thus, we find that the c-R3c GS of the $BiFeO_3$-$BiMnO_3$ nanocheckerboard is multiferroic: ferroelectric, with polarization comparable to the polarization of bulk $BiFeO_3$, and ferrimagnetic, with magnetization contributed by ferromagnetic ordering in the $BiMnO_3$ component.

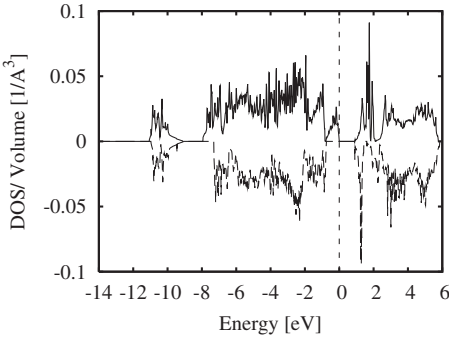

FIG. 9. Density of states (DOS) of the c-R3c FeAFMMnFM GS of $BiFeO_3$-$BiMnO_3$ nanocheckerboard. Spin up states are shown by a solid line and spin down states by a dashed line. The zero is set to the valence band maximum. The band gap in the spin-up channel is 0.9 eV.

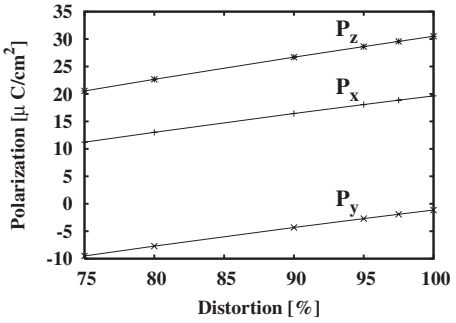

FIG. 10. Spontaneous polarization $\vec{P}=(P_x,P_y,P_z)$ as a function of the structural distortion of the c-R3c FeAFMMnFM $BiFeO_3$-$BiMnO_3$ nanocheckerboard. 100% distortion corresponds to the c-R3c ground state structure, and 0% to the ideal perovskite structure.

B. Magnetic coupling constants

To gain insight into the magnetic properties of the nanocheckerboard, we model the magnetic ordering energies using a nearest-neighbor (nn) Heisenberg model. The nn magnetic couplings arise from superexchange through the oxygens that lie on the bonds between the B-site cations, with the strength of the superexchange being quite sensitive to the geometry of the B-O-B? bond. If the structure were ideal cubic perovskite, there would be three independent couplings, J_{Fe}, J_{Mn}, and J_{int}, corresponding to 180° Fe-O-Fe, Mn-O-Mn, and Fe-O-Mn bonds, respectively. The analysis of the couplings in the c-R3c structure is based on the geometry of the B-O-B? bonds as given in Table IV; the labeling of the bonds and the changes in the bonds due to the $R_4^+([111])$ mode are shown in Fig. 11. The two Fe-O-Fe bonds are almost identical in bond angle and bond length; this is also the case for the two Mn-O-Mn bonds. This suggests that a single value of J_{Fe} and J_{Mn} can be used for the Fe-O-Fe and Mn-O-Mn interactions, respectively. On the other hand, the mixed Fe-O-Mn bonds vary in both B-O bond length, from 1.91–2.11 Å, and B-O-B bond angle, from 143.3–166.8°. This suggests the use of three different coupling constants J_{int}^{α}, J_{int}^{β} or J_{int}^{γ} for the Fe-O-Mn interactions based on the typical values of the bond angles, approxi-

TABLE IV. B-site-cation-oxygen-B-site-cation (B-O-B) bonds in the c-R3c ground state (GS) of the $BiFeO_3$-$BiMnO_3$ nanocheckerboard. B-O and O-B bond lengths and the B-O-B bond angle are given. Atoms are numbered as in Fig. 11. The subscript indicates the cartesian direction along which the bond lies.

B-O-B bond	Notation	|B-O| [Å]	|O-B| [Å]	Angle (deg)
$(Fe_1\text{-}O_7\text{-}Fe_2)_z$	J_{Fe}	1.93	2.08	153.8
$(Fe_2\text{-}O_5\text{-}Fe_1)_z$	J_{Fe}	1.96	2.08	156.8
$(Mn_1\text{-}O_8\text{-}Mn_2)_z$	J_{Mn}	2.10	1.91	153.7
$(Mn_2\text{-}O_6\text{-}Mn_1)_z$	J_{Mn}	1.87	2.18	156.3
$(Mn_1\text{-}O_1\text{-}Fe_1)_x$	J^{α}_{int}	1.92	2.06	166.8
$(Fe_1\text{-}O_2\text{-}Mn_1)_x$	J^{β}_{int}	1.97	1.97	156.8
$(Mn_1\text{-}O_3\text{-}Fe_1)_y$	J^{α}_{int}	1.95	1.95	165.1
$(Fe_1\text{-}O_4\text{-}Mn_1)_y$	J^{β}_{int}	2.04	1.91	155.3
$(Mn_2\text{-}O_9\text{-}Fe_2)_x$	J^{β}_{int}	2.05	2.03	152.0
$(Fe_2\text{-}O_{10}\text{-}Mn_2)_x$	J^{γ}_{int}	1.94	2.11	143.3
$(Mn_2\text{-}O_{11}\text{-}Fe_2)_y$	J^{β}_{int}	2.05	1.95	151.1
$(Fe_2\text{-}O_{12}\text{-}Mn_2)_y$	J^{γ}_{int}	2.07	1.98	144.1

mately 166°, 154°, and 144°, respectively. Note that the angles of the Fe-O-Mn bonds in the Fe_1-Mn_1 layer in Fig. 11 are about 166° and 154°, while the angles in the Fe_2-Mn_2 layer are about 152° and 144°.

The values of these five exchange couplings were determined from first-principles results for the total energies of various magnetic orderings for the c-R3c GS structure of the nanocheckerboard, given in Table V. The structure is fixed to that obtained for the FeAFMMnFM ordering $Fe_1^{\uparrow}Fe_2^{\downarrow}Mn_1^{\uparrow}Mn_2^{\uparrow}$. The ordering $Fe_1^{\downarrow}Fe_2^{\uparrow}Mn_1^{\uparrow}Mn_2^{\uparrow}$, also described as FeAFMMnFM, is a distinct state with a different (higher) energy. Similarly, for the FeFMMnAFM ordering, there are two distinct magnetic states: $Fe_1^{\uparrow}Fe_2^{\uparrow}Mn_1^{\downarrow}Mn_2^{\uparrow}$ and $Fe_1^{\uparrow}Fe_2^{\uparrow}Mn_1^{\uparrow}Mn_2^{\downarrow}$, with different energies as given in Table V.

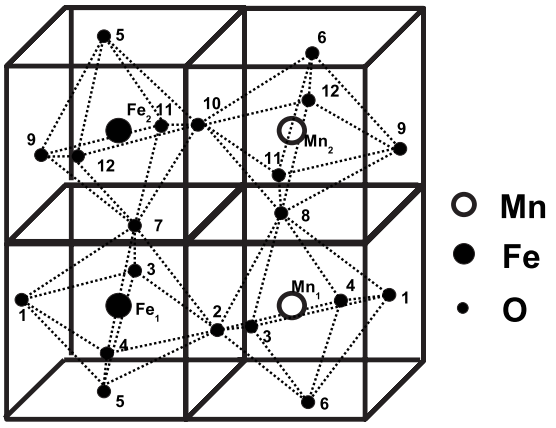

FIG. 11. Sketch showing the displacements of oxygen atoms in the $R_4^+([111])$ mode, which contributes to the c-R3c GS of the $BiFeO_3$-$BiMnO_3$ nanocheckerboard. Two inequivalent iron (Fe_1 and Fe_2) and manganese (Mn_1 and Mn_2) atoms and twelve oxygens (1–12) comprise the $\sqrt{2}\times\sqrt{2}\times 2$ unit cell. The corners of each cube are occupied by Bi (not shown).

We express the Heisenberg magnetic energy of each magnetic state,

$$E = E_0 + \frac{1}{2}\sum_{ij} J_{ij} S_i S_j, \tag{4}$$

where S_i and S_j are the spins $S_{Fe}=\frac{5}{2}$, $S_{Mn}=\frac{4}{2}$ with coupling constants $J_{ij}=J_{Fe}$, J_{Mn}, J^{α}_{int}, J^{β}_{int}, J^{γ}_{int}, and E_0 is a constant. We extract values of the coupling constants by fitting the Heisenberg model energy to the first-principles energies by the least-squares method, obtaining

$$E_0 = 218 \text{ meV}, \quad J_{Fe} = 7.1 \text{ meV}, \quad J_{Mn} = -3.2 \text{ meV},$$

$$J^{\alpha}_{int} = -3.0 \text{ meV}, \quad J^{\beta}_{int} = 4.3 \text{ meV}, \quad J^{\gamma}_{int} = 7.3 \text{ meV}. \tag{5}$$

The quality of the fit can be assessed by comparing the first-principles energy to the fitted values in the fifth column of the table.

The AFM character of J_{Fe} and the FM character of J_{Mn} correspond to that of bulk G-AFM $BiFeO_3$ and bulk FM $BiMnO_3$, respectively. Their values are comparable to those obtained from the observed bulk transition temperatures within mean field theory assuming a single J: $J_{Fe,bulk} \approx 6.3$ meV and $J_{Mn,bulk} \approx -1.5$ meV, respectively.[65–70] The correspondence is not exact because of the difference in the bond geometry between bulk $BiFeO_3$ and bulk $BiMnO_3$ and the nanocheckerboard.

In the Fe_1-Mn_1 layer, the average Fe-Mn interaction J_{int} is very weakly AFM $(J^{\alpha}_{int}+J^{\beta}_{int})/2 \gtrsim 0$, while in the Fe_2-Mn_2 layer it is strongly AFM $(J^{\beta}_{int}+J^{\gamma}_{int})/2 > 0$. This corresponds to the preferred FeAFMMnFM ordering $Fe_1^{\uparrow}Fe_2^{\downarrow}Mn_1^{\uparrow}Mn_2^{\uparrow}$ and explains the close competition with G-AFM ordering, in which both layers are AFM ordered (see Fig. 3 and Table V). The exchange coupling between d^5 Fe and d^4 Mn takes place via superexchange through the bridging O. For angles close to 180°, strong σ bonding favors FM ordering. However, as the Fe-O-Mn angles deviate from 180° through the oxygen octahedron rotational distortion, the admixture of π bonding leads to an increasingly AFM character of the coupling.[52–54] This behavior can be seen in the dependence of the fitted values for J_{int} on the Fe-O-Mn angle, plotted in Fig. 12.

Within this nearest-neighbor Heisenberg model, we explored a wider range of possible magnetic orderings for the R3c structure nanocheckerboard, in particular, orderings with lower translational symmetry than those included in the first-principles investigation. The supercells considered included $2\times2\times2$ ($p=8$ perovskite cells), $2\times2\times4$ and $4\times2\times2$ ($p=16$ perovskite unit cells). The Heisenberg model energies were computed for all 2^p spin configurations in each supercell.

The lowest energy ordering found in this larger set of configurations is still the FeAFMMnFM ordering, with FM alignment of the Mn and AFM antialignment of the Fe along the Mn and Fe pillars, respectively, and alternating FM and AFM xy layers as in Fig. 3. The lowest-energy alternative magnetic state is a state in which one Mn per supercell in the

TABLE V. Calculated magnetic energies ΔE per four-perovskite unit cell (u.c.) in the c-R3c GS structure of $BiFeO_3$-$BiMnO_3$ nanocheckerboard. The notation for magnetic ordering is that of Fig. 3. The symbols x, y, a, b, c appearing in the magnetic energy are defined as follows: $x=J_{Fe}S_{Fe}S_{Fe}$, $y=J_{Mn}S_{Mn}S_{Mn}$, $a=J^{\alpha}_{int}S_{Fe}S_{Mn}$, $b=J^{\beta}_{int}S_{Fe}S_{Mn}$, and $c=J^{\gamma}_{int}S_{Fe}S_{Mn}$.

Magnetic state	Magnetic ordering	Heisenberg energy [per u.c.]	ΔE [eV/u.c.]	Fitted ΔE [eV/u.c.]
FeAFMMnFM	$Fe_1^{\uparrow}Fe_2^{\downarrow}Mn_1^{\uparrow}Mn_2^{\uparrow}$	$E_0-2x+2y+2a-2c$	0.000	0.000
FeAFMMnFM	$Fe_1^{\downarrow}Fe_2^{\uparrow}Mn_1^{\uparrow}Mn_2^{\uparrow}$	$E_0-2x+2y-2a+2c$	0.200	0.207
G-AFM	$Fe_1^{\uparrow}Fe_2^{\downarrow}Mn_1^{\downarrow}Mn_2^{\uparrow}$	$E_0-2x-2y-2a-4b-2c$	0.032	0.026
C-AFM	$Fe_1^{\uparrow}Fe_2^{\uparrow}Mn_1^{\downarrow}Mn_2^{\downarrow}$	$E_0+2x+2y-2a-4b-2c$	0.143	0.152
FeFMMnAFM	$Fe_1^{\uparrow}Fe_2^{\uparrow}Mn_1^{\downarrow}Mn_2^{\uparrow}$	$E_0+2x-2y-2a+2c$	0.436	0.436
FeFMMnAFM	$Fe_1^{\uparrow}Fe_2^{\uparrow}Mn_1^{\uparrow}Mn_2^{\downarrow}$	$E_0+2x-2y+2a-2c$	0.222	0.229
FeAFMMnAFM	$Fe_1^{\uparrow}Fe_2^{\downarrow}Mn_1^{\uparrow}Mn_2^{\downarrow}$	$E_0-2x-2y+2a+4b+2c$	0.275	0.284
FM	$Fe_1^{\uparrow}Fe_2^{\uparrow}Mn_1^{\uparrow}Mn_2^{\uparrow}$	$E_0+2x+2y+2a+4b+2c$	0.416	0.410

FM xy layer flips, at an energy cost of 6.3 meV/supercell. The net magnetization for the resulting state decreases from $M_{GS}=3.8\mu_B$ per one Fe-Mn pair to $\frac{p-2}{p}M_{GS}$.

Within a mean field approximation with four effective fields, two for the two Fe atoms and two for the two Mn atoms in the unit cell of the $BiFeO_3$-$BiMnO_3$ nanocheckerboard, the magnetic transition temperature of the $BiFeO_3$-$BiMnO_3$ nanocheckerboard is $T_c=406$ K. This temperature is intermediate between the Neel temperature, $T_N^{exp}=643$ K, of bulk $BiFeO_3$ and the Curie temperature, $T_c^{exp}=105$ K, of bulk $BiMnO_3$.[65–69]

VI. ALTERNATIVE STRUCTURES OF THE $BIFEO_3$-$BIMNO_3$ NANOCHECKERBOARD

The energies for various magnetic orderings and structural distortions of the nanocheckerboard are shown in Fig. 13. The structural parameters for each structure type are relaxed for each magnetic ordering. The most energetically favorable alternative structures, like the ground state FeAFMMnFM c-R3c structure, are polar and include oxygen octahedra rotations.

The polar distortion in the alternative structures of the nanocheckerboard is quantified by the value of the polarization computed using nominal charges [Eq. (2)], that can be directly compared with nominal-charge polarizations in the structures of $BiFeO_3$ (cf. Tables II and VI). As in $BiFeO_3$, there is a low-lying supertetragonal P4mm phase, with $c/a \sim 1.3$ and very large spontaneous polarization. For the various structures considered, the polarization tends to decrease as rotational distortion is introduced, with the smallest value found in the c-R3c structure.

In the P4/mmm structure, the nanocheckerboard is metallic, while a band gap opens with either polar or rotational distortion. This behavior is similar to that of $BiMnO_3$ and $BiFeO_3$, which are metallic in the FM $Pm\bar{3}m$, or P4/mmm structures with a band gap opened and/or widened by distortion (in FM $BiMnO_3$, only in the spin-down channel).

As can be seen in Fig. 13, the difference in energies between different structure types is generally much larger than the difference in magnetic energies for a given structure type. The interesting feature of this figure is that the favored magnetic ordering is different for different structure types, switching between ferrimagnetic FeAFMMnFM and antiferromagnetic G-AFM. This is in contrast to the case of bulk $BiFeO_3$ (see Fig. 6), or bulk $BiMnO_3$ (see Fig. 8), in which

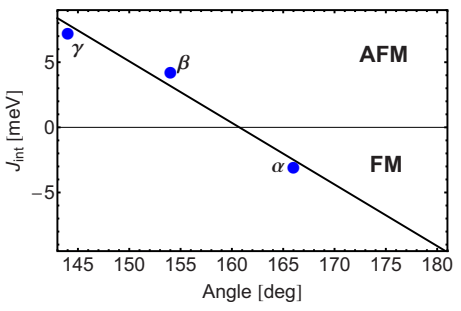

FIG. 12. (Color online) Angular dependence of the Fe-Mn magnetic exchange coupling constant J_{int} in the c-R3c GS structure of the $BiFeO_3$-$BiMnO_3$ nanocheckerboard (blue circles). The black line is a linear fit. J_{int} changes sign (AFM $J_{int}>0$ to FM $J_{int}<0$) at the bond angle of 160°.

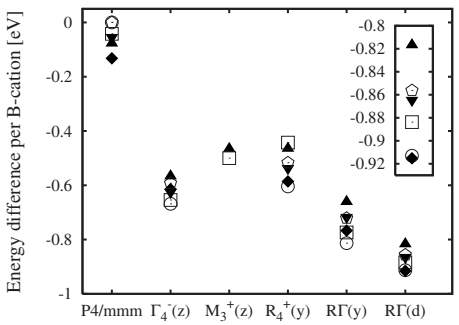

FIG. 13. Structural energetics of $BiFeO_3$-$BiMnO_3$ nanocheckerboard. Energy difference per perovskite cell (per B-cation) for different magnetic orderings (see Fig. 3) and for structural distortions (see Fig. 4 and Table I). Inset: zoomed view of the magnetic energies for the c-R3c structure. FeAFMMnFM ordering (filled diamond) competes with G-AFM ordering (open circle) in the nanocheckerboard alternative structures.

TABLE VI. Low-energy alternative and ground state (GS) structure of $BiFeO_3$-$BiMnO_3$ nanocheckerboard. Energy difference ΔE[eV/B-cation] is calculated for different magnetic orderings with respect to FeAFMMnAFM P4/mmm structure [as in Fig. 13]. Insulating DOS band gap Δ (or metallic m character), polarization P estimated from the nominal charges [Eq. (2)], the in-plane a and out-of-plane c lattice constants [see perovskite cell in Fig. 1], and oxygen-octahedron rotation angle Θ are given for the lowest-energy magnetic ordering corresponding to each structural distortion.

Space group	P4/mmm	c-P4mm	c-I4cm	c-R3c
Modes		$\Gamma_4^-(z)$	R_4^+ , $\Gamma_4^-(y)$	R_4^+ , $\Gamma_4^-([111])$
Mag. order	FeAFMMnFM	G-AFM	G-AFM	FeAFMMnFM
Δ [eV]	m	1.01	1.55	0.90
P [μC/cm^2]		101.9	71.5	57.9
a/c [Å]	3.81/3.88	3.66/4.60	5.80/3.67	5.50/3.93
Θ[°]			4.8	7.2–20.3
ΔE (FeAFMMnFM)	−0.132	−0.615	−0.767	−0.915
ΔE (G-AFM)	0.000	−0.668	−0.813	−0.913
ΔE (C-FIM)	−0.042	−0.654	−0.774	−0.884
ΔE (FeFMMnAFM)	−0.054	−0.625	−0.717	−0.865
ΔE (FeAFMMnAFM)	0.000	−0.592	−0.721	−0.856
ΔE (FM)	−0.077	−0.567	−0.661	−0.817

the favored magnetic ordering does not change for different structure types.

VII. MAGNETIC AND STRUCTURAL TRANSITIONS DRIVEN BY ANISOTROPIC STRAIN

The sensitivity of the magnetic exchange couplings to the structure should produce changes in the magnetic ordering energies for perturbations that couple to the crystal structure, such as electric field, pressure and epitaxial strain. It is even possible that a structural perturbation could drive the system through a magnetic transition into an alternative low-energy ordering. Furthermore, the fact that in the nanocheckerboard the favored magnetic ordering is different for different structure types, discussed in the previous section, suggests that the magnetic ordering of the system could in principle be changed by a perturbation that changes the structure type, producing a novel magnetic-coupling response at the magnetic-structural phase boundary.[25,32] For example, it might be possible to drive the nanocheckerboard from its ferrimagnetic FeAFMMnFM c-R3c GS with a nonzero magnetization to a G-AFM c-I4cm state with zero magnetization.

We have explored this possibility for two types of epitaxial strain. First, we investigated the c-R3c phase with an isotropic epitaxial strain, corresponding to an (110) matching plane. Thus, the second and third lattice vectors of the $\sqrt{2}a \times \sqrt{2}a \times 2c$ supercell, along [−110] and along [001], are constrained to be perpendicular with uniform scaling of the lattice constants $a=(1+s)a_0$ and $c=(1+s)c_0$, where $a_0=5.50$ Å and $c_0=3.93$ Å are the unstrained lattice constants of FeAFMMnFM c-R3c GS. In this case, there is no magnetic transition: the system remains FeAFMMnFM from $s=0\%$ up to strain of 10%.

Second, we considered an anisotropic epitaxial strain, corresponding to a (001) matching plane, such that the lattice constant along [110] is fixed to $\sqrt{2}\times a_0=5.52$ Å, while the lattice constant a? along [−110] is elongated, with strain defined as $\frac{a?-a_0}{a_0}$. $a_0=3.9$ Å is chosen as it is the lattice constant of an ideal perovskite cell with volume which is the average of that of bulk R3c $BiFeO_3$ ($V_{BFO}=59.28$ Å^3/B-cation) and bulk C2/c[71,72] $BiMnO_3$ ($V_{BMO}=59.41$ Å^3/B-cation).

The anisotropic epitaxial strain dependence of the energies of the c-R3c and c-I4m structures is presented in Fig. 14. At 0% strain, the energy difference between FeAFMMnFM to G-AFM in the c-R3c structure is 5 meV/B-cation; this differs slightly from the value for the relaxed structures reported in Table VI due to the difference in lattice constants between the epitaxial constrained structure and the fully relaxed structure (the corresponding energy difference at 0% strain for c-I4cm is greater because the difference in lattice constants is greater). At 3% strain, there is a magnetic transition from ferrimagnetic FeAFMMnFM to this low-lying

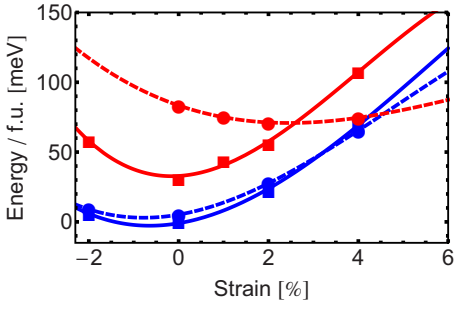

FIG. 14. (Color online) Epitaxial-strain-driven magnetic transition in $BiFeO_3$-$BiMnO_3$ nanocheckerboard. Total energies of the FeAFMMnFM (solid) and G-AFM (dashed line) magnetic orderings in the c-R3c structure type (blue) and c-I4cm structure type (red), as a function of anisotropic in-plane tensile strain (details in the text).

TABLE VII. Calculated total magnetic energies and energy differences in an ideal perovskite structure with lattice constant a_0 =3.839 Å for various magnetic states in the checkerboard, rocksalt (oxygens are relaxed to accommodate their preferable positions), and layered superlattice of $BiFeO_3$-$BiMnO_3$. The checkerboard ordering shows a quasidegenerate (or pseudodegenerate) spectrum of magnetic energies, whereas the rocksalt and layered superlattice show larger gaps between the ground state (GS) and the first alternative magnetic state. Values of $U_{Fe}=U_{Mn}=5$ eV and $J_{Fe}=J_{Mn}=1$ eV are used in the first, and $U^{eff}_{Fe}=4$ eV, $U^{eff}_{Mn}=5.2$ eV with $U^{eff}=U-J$ in the second column (see Sec. II).

Checkerboard	E [eV/B-cation]	Rocksalt superlattice	E [eV/B-cation]	Layered superlattice	E [eV/B-cation]
Magnetic state		Magnetic state		Magnetic state	
FeAFMMnFM	−35.04, −34.68	FMFM	−35.06, −34.66	FeAFMMnFM	−35.11, −34.76
	ΔE [eV/B-cation]		ΔE [eV/B-cation]		ΔE [eV/B-cation]
FeAFMMnFM	0.000, 0.000	FMFM	0.000, 0.000	FeAFMMnFM	0.000, 0.000
FM	0.022, 0.028	FeAFMMnFM	0.044, 0.070	FM	0.111, 0.097
C-FIM	0.076, 0.113	FeFMMnAFM	0.045, 0.055	FeFMMnFM	0.136, 0.143
FeAFMMnAFM	0.081, 0.084	FM	0.065, 0.047	FeAFMMnAFM	0.135, 0.137
G-AFM	0.114, 0.152	AFMAFM	0.101, 0.084	G-AFM	0.181, 0.219
FeFMMnAFM	0.119, 0.129	G-AFM	0.114, 0.079	FeFMMnAFM	0.260, 0.257

G-AFM phase, while the structure remains c-R3c. This arises from the modification of the exchange couplings by the structural changes produced by the changing epitaxial strain.

With a further increase in strain, there is a transition from c-R3c to a c-I4cm phase at about 4.5%. Since the favored magnetic ordering is G-AFM in both structural phases, no magnetic transition accompanies the structural transition. However, this result does illustrate the feasibility of an epitaxial-strain-induced structural transition from one pattern of rotational distortions to another in this system; a coupled structural-magnetic phase boundary thus may be brought to light by future exploration of various epitaxial strain constraints.

VIII. ROLE OF THE B-SITE CATION ORDERING IN MAGNETOSTRUCTURAL EFFECT

Pseudodegenerate (or quasidegenerate) magnetic states in the $BiFeO_3$-$BiMnO_3$ nanocheckerboard are a necessary ingredient for the observed magnetostructural effect (cf. Figure 13 and Table VI), where change in the magnetic ordering is achieved by a perturbation (e.g., epitaxial strain, as in Sec. VII). Here, we investigate the role of the cation-ordering geometry in determining the spectrum of magnetic states; in particular, this will show whether the quasidenerature spectrum is unique to the checkerboard geometry.

Magnetic energies are computed in the ideal perovskite structures of five systems: the bulk parent $BiFeO_3$ and $BiMnO_3$, the $BiFeO_3$-$BiMnO_3$ nanocheckerboard, the $BiFeO_3$-$BiMnO_3$ layered (001) superlattice, and the $BiFeO_3$-$BiMnO_3$ rocksalt structure with Fe and Mn alternating in every other unit cell ((111) superlattice). The results for the checkerboard, the rocksalt, and the layered superlattice are presented in Table VII. Bulk $BiFeO_3$ and bulk $BiMnO_3$ exhibit behavior similar to the (001) layered superlattice.[32] In these three systems, the difference in energy between the magnetic ground state (G-AFM in bulk $BiFeO_3$, FM in bulk $BiMnO_3$, and FeAFMMnFM in the (001) layered superlattice) and the first alternative state is in the range 0.10–0.14 eV/B-cation. This spectral gap is sufficiently large that structural changes cannot lower the energy of an alternative state below that of the original magnetic ground state.

Indeed, for all structures considered the lowest magnetic state in bulk $BiFeO_3$ and bulk $BiMnO_3$ is G-AFM and FM, respectively (see Figs. 6 and 8). In the (001) superlattice, we calculate magnetic energies for the G-AFM and FeAFMMnFM magnetic states in two structural distortions: For l-I4cm (see Table I), we find $\Delta E=-0.504$ eV/B-cation for G-AFM and $\Delta E=-0.553$ eV/B-cation for FeAFMMnFM with respect to the FeAFMMnFM magnetic state in the ideal perovskite cell (see Table VII). For l-R3c, we find $\Delta E=-0.752$ eV/B-cation for G-AFM and $\Delta E=-0.761$ eV/B-cation for FeAFMMnFM. For both structural distortions considered, the lowest energy magnetic ordering is FeAFMMnFM.

In contrast, all magnetic states in the nanocheckerboard are quasidegenerate, all are lower in energy than the lowest-energy states in the (001) superlattice and the bulk. The rocksalt structure is an intermediate case: while the difference between the FMFM magnetic ground state and the first alternative state is 0.05 eV/B-cation, close to half of the spectral gap of the (001) superlattice and bulk, all the states considered fall in the same low-energy window as for the checkerboard. Therefore, it is much more likely that a structurally driven transition between the different magnetic states could occur in the checkerboard, or in the rocksalt structure, than in the other geometries studied here.

The importance of the B-site cation geometry in the magnetic ordering energy spectrum can be qualitatively understood from a simple Heisenberg model of the form given in Eq. (4), where we assume that the exchange couplings J_{Fe}, J_{Mn} and J_{int} are independent of cation geometry, thus being

transferable from one geometry to the other. We can approximately reproduce the magnetic ordering energies in the ideal perovskite structure of the checkerboard with the Mn-Mn interaction J_{Mn} being strongly FM, the Fe-Fe interaction J_{Fe} being AFM and about half the strength, and the Fe-Mn interaction J_{int} being weakly FM. Assuming the same values in the FeAFMMnFM GS of the (001) layered superlattice, the high and medium-strength bonds are all satisfied (?happy? in the language of frustrated magnetism) and the only unhappy bonds are weak bonds between the Mn and the

opposite spin Fe in the adjacent layer (one bond per B cation). Thus this state is energetically clearly preferred over other orderings considered, which all involve a significant fraction of unhappy high and/or medium strength bonds, thus opening the observed gap in the magnetic energy spectrum. In contrast, in the checkerboard, the total fraction of high and medium-strength bonds is half that in the layered superlattice, and the alternative states are low in energy as they involve tradeoffs between a larger number of happy weak bonds and a smaller number of unhappy medium or high-strength bonds. Finally, in the rocksalt structure, all the nearest neighbor bonds are weak. This is consistent with the fact that all orderings considered are at low energies. However, a simple one-parameter model does not correctly account for the energetic order of the states in this range or the gap between the ground state ordering and the first alternative state, which would require a model including next-nearest neighbor interactions.

Indeed, the assumption of exact transferability used above is only semiquantitatively valid. In particular, changes in B-site cation geometry result in relative energy shifts of the Fe, Mn, and O states and changes in the orbital wave functions, and thus in changes to the wave function overlaps and energy denominators that contribute to superexchange. This leads to different values of the magnetic couplings J_{Fe}, J_{Mn}, or J_{int} in the various geometries considered (cf. Table VII). In addition, structural distortions modify these magnetic couplings, as would be needed to explain the difference in the ordering of the magnetic energies in Tables VI and VII. However, the simple model does serve to give useful insight into this complex issue, and highlights the fact that the magnetic ordering spectrum is indeed very sensitive to the B-site cation arrangement.

IX. DISCUSSION

The experimental realization of the $BiFeO_3$-$BiMnO_3$ nanocheckerboard would be challenging as its formation energy is positive: the combined total energies of R3c G-AFM ground state of bulk $BiFeO_3$ ($E[BFO]=-35.079$ eV/B-cation) and of the R3c FM lowest energy structure of bulk $BiMnO_3$ ($E[BMO]=-36.676$ eV/B-cation) are lower than that of the c-R3c FeAFMMnFM ground state of the $BiFeO_3$-$BiMnO_3$ nanocheckerboard ($E[BFMO]=-71.694$ eV/2B-cations). Though the $BiFeO_3$-$BiMnO_3$ nanocheckerboard is at best metastable, there is indication from experiments that fabrication of the $BiFeO_3$-$BiMnO_3$ nanocheckerboard with square sizes on the order of a unit cell would not be impossible with appropriate tuning of growth parameters. Growth of (001) $BiMnO_3$ on $BiFeO_3$ films has recently been reported. In this study post-annealing led to intermixing of the Fe and Mn, with a concomitant increase in ferromagnetic T_c.[73] This experiment provides support for the first-principles observation that magnetic ordering in this system is very sensitive to the B-site cation arrangement. With regard to other film orientations, (110) and (111) as well as (001) $BiFeO_3$ films have been successfully grown on oriented $SrTiO_3$ substrates.[74,75] For $BiMnO_3$, (111) and (001) oriented films have been grown with substrate vicinality.[76,77] There should be no fundamental obstacle to analogous growth of (110) oriented films of $BiMnO_3$. More generally, a combination of patterned substration, possible masking, layer-by-layer growth, and carefully tuned growth parameters could influence the deposition process enough to produce a checkerboard structure of $BiFeO_3$-$BiMnO_3$.

In order to make better contact with future experiment, it is useful to consider magnetic ordering of larger-scale $n \times n$ $BiFeO_3$-$BiMnO_3$ checkerboards, where the lateral dimension of the $BiFeO_3$ and $BiMnO_3$ pillars is n perovskite lattice constants. Within each pillar, $BiFeO_3$ and $BiMnO_3$ regions should be G-AFM and FM respectively, since this ordering is the most energetically favorable in the parent bulk structures. This is true even in the extreme case of n=1 discussed in Sec. V. The magnetic coupling constants J_{Fe}, J_{Mn} and J_{int} [Eq. (5)], obtained in Sec. V B would allow the construction of Heisenberg models to explore the magnetic ordering of these larger-scale checkerboards with the ideal perovskite structure, where J_{Fe} and J_{Mn} connecting two atoms in the xy plane can be taken to be equal to the coupling along the pillar, but we have not pursued this farther here. Generally speaking, we expect that the possibility of a structurally driven magnetic transition should decrease as the lateral size of the $BiFeO_3$ and $BiMnO_3$ pillars increases and the interface effects (Fe-Mn interactions) become less important.

On a technical note, the robustness of our calculated first-principles results has been checked by using two different implementations of LSDA+U with different parametrizations to compute magnetic ordering energies in the ideal perovskite structure for the checkerboard, the rocksalt cation ordering, and the layered superlattice (Table VI). The key results are the same for both implementations: the type of ground state magnetic ordering for each cation arrangement, the quasidegeneracy of the spectrum of magnetic energies in the checkerboard, the gap in the energy spectrum in the layered (001) superlattice, and the intermediate character of the rocksalt ordering.

Finally we remark that our first principles calculations do not include spin-orbit coupling (SOC) that is known to lead to weak ferromagnetism in $BiFeO_3$.[78] Since the $BiFeO_3$-$BiMnO_3$ nanocheckerboard already has a ferrimagnetic ground state without SOC, inclusion of SOC may result in a slightly changed value of the total magnetization and to small canting angles of the Fe and Mn spins; these changes should not fundamentally affect the results presented here. The addition of SOC to our present calculations is certainly worth pursuing in future work.

X. SUMMARY

In this paper, the structure and properties of an atomic-scale $BiFeO_3$-$BiMnO_3$ checkerboard were investigated using first-principles calculations and magnetic modeling. This unusual heterostructure was found to have properties distinct from those of its bulk parent constituents, or those of (001) superlattices of these two materials. We attribute this behavior to the magnetic frustration resulting from its B-site cation geometry; this leads to a quasidegenerate manifold of magnetic states that can be switched through small applied external perturbations, resulting in an unusual magnetostructural effect. The possibility of realizing this system in the laboratory was discussed. This study of a two-component nanocheckerboard should be considered as a proof-of-principle example, and we plan to study similar geometries on longer length scales to facilitate contact with future experiments.

ACKNOWLEDGMENTS

We thank E. Bousquet, V. R. Cooper, M. Dawber, J. Driscoll, C. Ederer, C.-J. Eklund, C. J. Fennie, M. S. Hybertsen, J. H. Lee, A. Malashevich, M. Marsman, J. B. Neaton, T. Nishimatsu, S. Patnaik, O. Paz, D. R. Reichman, N. A. Spaldin, D. Vanderbilt, C. G. Van de Walle, and K. B. Whaley for helpful discussions. This work was supported in part by NSF MRSEC (Grant No. DMR-0820404), NSF (Grant No. NIRT-ECS-0608842) and by the U.S. Army Research Office through (Grant No. W911NF-07-0410).

[1] A. Ohtomo, D. A. Muller, J. L. Grazul, and H. Y. Hwang, Nature (London) **419**, 378 (2002).
[2] J. B. Neaton and K. M. Rabe, Appl. Phys. Lett. **82**, 1586 (2003).
[3] C. H. Ahn, K. M. Rabe, and J.-M. Triscone, Science **303**, 488 (2004).
[4] D. D. Fong, G. B. Stephenson, S. K. Streiffer, J. A. Eastman, O. Auciello, P. H. Fuoss, C. Thompson, A. Ohtomo, D. A. Muller, J. L. Grazul, and H. Y. Hwang, Science **304**, 1650 (2004).
[5] K. Johnston, X. Huang, J. B. Neaton, and K. M. Rabe, Phys. Rev. B **71**, 100103(R) (2005).
[6] M. Dawber, K. M. Rabe, and J. F. Scott, Rev. Mod. Phys. **77**, 1083 (2005).
[7] K. M. Rabe, Curr. Opin. Solid State Mater. Sci. **9**, 122 (2005).
[8] M. Dawber, C. Lichtensteiger, M. Cantoni, M. Veithen, P. Ghosez, K. Johnston, K. M. Rabe, and J.-M. Triscone, Phys. Rev. Lett. **95**, 177601 (2005).
[9] H. N. Lee, H. M. Christen, M. F. Chisholm, C. M. Rouleau, and D. H. Lowndes, Nature (London) **433**, 395 (2005).
[10] S. M. Nakhmanson, K. M. Rabe, and D. Vanderbilt, Phys. Rev. B **73**, 060101(R) (2006).
[11] R. Ramesh and D. G. Schlom, Science **296**, 1975 (2002).
[12] C. Cen, S. Thiel, J. Mannhart, and J. Levy, Science **323**, 1026 (2009).
[13] J. Mannhart and D. G. Schlom, Science **327**, 1607 (2010).
[14] H. Zheng, J. Wang, S. E. Lofland, Z. Ma, L. Mohaddes-Ardabili, T. Zhao, L. Salamanca-Riba, S. R. Shinde, S. B. Ogale, F. Bai, D. Viehland, Y. Jia, D. G. Schlom, M. Wuttig, A. Roytburd, and R. Ramesh, Science **303**, 661 (2004).
[15] J. L. MacManus-Driscoll, P. Zerrer, H. Wang, H. Yang, J. Yoon, A. Fouchet, R. Yu, M. G. Blamire, and Q. Jia, Nature Mater. **7**, 314 (2008).
[16] S. Yeo, Y. Horibe, S. Mori, C. M. Tseng, C. H. Chen, A. G. Khachaturyan, C. L. Zhang, and S.-W. Cheong, Appl. Phys. Lett. **89**, 233120 (2006).
[17] C. L. Zhang, S. Yeo, Y. Horibe, Y. J. Choi, S. Guha, M. Croft, S.-W. Cheong, and S. Mori, Appl. Phys. Lett. **90**, 133123 (2007).
[18] C. L. Zhang, C. M. Tseng, C. H. Chen, S. Yeo, Y. J. Choi, and S.-W. Cheong, Appl. Phys. Lett. **91**, 233110 (2007).
[19] B. S. Guiton and P. K. Davies, Nature Mater. **6**, 586 (2007).
[20] J. F. Scott, Nature Mater. **6**, 256 (2007).
[21] C. A. F. Vaz, J. Hoffman, C. H. Ahn, and R. Ramesh, Adv. Mater. **22**, 2900 (2010).
[22] D. P. Kozlenko, V. P. Glazkov, R. A. Sadykov, B. N. Savenko, V. I. Voronin, and I. V. Medvedeva, J. Magn. Magn. Mater. **258-259**, 290 (2003).
[23] J. H. Lee and K. M. Rabe, Phys. Rev. Lett. **104**, 207204 (2010).
[24] T. Murata, H. Kushida, T. Terai, and T. Kakeshita, J. Magn. Magn. Mater. **310**, 1555 (2007).
[25] C. J. Fennie and K. M. Rabe, Phys. Rev. Lett. **97**, 267602 (2006).
[26] R. T. Lechner, G. Springholz, T. U. Schülli, J. Stangl, T. Schwarzl, and G. Bauer, Phys. Rev. Lett. **94**, 157201 (2005).
[27] J. M. Rondinelli, M. Stengel, and N. A. Spaldin, Nat. Nanotechnol. **3**, 46 (2008).
[28] N. A. Hill, J. Phys. Chem. B **104**, 6694 (2000).
[29] C.-W. Nan, M. I. Bichurin, S. Dong, D. Viehland, and G. Srinivasan, J. Appl. Phys. **103**, 031101 (2008).
[30] R. Ramesh and N. A. Spaldin, Nature Mater. **6**, 21 (2007).
[31] P. Baettig and N. A. Spaldin, Appl. Phys. Lett. **86**, 012505 (2005).
[32] L. Pálová, P. Chandra, and K. M. Rabe, Phys. Rev. Lett. **104**, 037202 (2010).
[33] G. Kresse and J. Hafner, Phys. Rev. B **47**, 558 (1993).
[34] G. Kresse and J. Furthmuller, Phys. Rev. B **54**, 11169 (1996).
[35] P. E. Blochl, Phys. Rev. B **50**, 17953 (1994).
[36] G. Kresse and D. Joubert, Phys. Rev. B **59**, 1758 (1999).
[37] A. I. Liechtenstein, V. I. Anisimov, and J. Zaanen, Phys. Rev. B **52**, R5467 (1995).
[38] S. L. Dudarev, G. A. Botton, S. Y. Savrasov, C. J. Humphreys, and A. P. Sutton, Phys. Rev. B **57**, 1505 (1998).
[39] J. B. Neaton, C. Ederer, U. V. Waghmare, N. A. Spaldin, and K. M. Rabe, Phys. Rev. B **71**, 014113 (2005).
[40] P. Baettig, R. Seshadri, and N. A. Spaldin, J. Am. Chem. Soc. **129**, 9854 (2007).
[41] I. Sosnowska, W. Schäfer, W. Kockelmann, K. H. Andersen, and I. O. Troyanchuk, Appl. Phys. A: Mater. Sci. Process. **74**, s1040 (2002).
[42] H. J. Monkhorst and J. D. Pack, Phys. Rev. B **13**, 5188 (1976).
[43] P. E. Blochl, O. Jepsen, and O. K. Andersen, Phys. Rev. B **49**,

16223 (1994).
[44] H. T. Stokes, E. H. Kisi, D. M. Hatch, and C. J. Howard, Acta Crystallogr., Sect. B: Struct. Sci. **58**, 934 (2002).
[45] R. D. King-Smith and D. Vanderbilt, Phys. Rev. B **47**, 1651 (1993).
[46] R. Resta and D. Vanderbilt, *Physics of Ferroelectrics: A Modern Perspective* (Springer-Verlag, Berlin, 2007), pp. 31–68.
[47] N. Marzari and D. Vanderbilt, Phys. Rev. B **56**, 12847 (1997).
[48] O. Paz and K. M. Rabe (private communication).
[49] C. Michel, J.-M. Moreau, G. D. Achenbach, R. Gerson, and W. J. James, Solid State Commun. **7**, 701 (1969).
[50] F. Kubel and H. Schmid, Acta Crystallogr., Sect. B: Struct. Sci. **46**, 698 (1990).
[51] S. Coh, T. Heeg, J. H. Haeni, M. D. Biegalski, J. Lettieri, L. F. Edge, K. E. O'Brien, P. Reiche, R. Uecker, S. Trolier-McKinstry, D. G. Schlom, and D. Vanderbilt, Phys. Rev. B **82**, 064101 (2010).
[52] J. B. Goodenough, Phys. Rev. **100**, 564 (1955).
[53] J. Kanamori, J. Phys. Chem. Solids **10**, 87 (1959).
[54] J. H. Lee and K. M. Rabe (private communication).
[55] C. Ederer and N. A. Spaldin, Phys. Rev. Lett. **95**, 257601 (2005).
[56] A. J. Hatt, N. A. Spaldin, and C. Ederer, Phys. Rev. B **81**, 054109 (2010).
[57] R. J. Zeches, M. D. Rossell, J. X. Zhang, A. J. Hatt, Q. He, C.-H. Yang, A. Kumar, C. H. Wang, A. Melville, C. Adamo, G. Sheng, Y.-H. Chu, J. F. Ihlefeld, R. Erni, C. Ederer, V. Gopalan, L. Q. Chen, D. G. Schlom, N. A. Spaldin, L. W. Martin, and R. Ramesh, Science **326**, 977 (2009).
[58] T. Atou, H. Chiba, K. Ohoyama, Y. Yamaguchi, and Y. Syono, J. Solid State Chem. **145**, 639 (1999).
[59] A. Moreira dos Santos, A. K. Cheetham, T. Atou, Y. Syono, Y. Yamaguchi, K. Ohoyama, H. Chiba, and C. N. R. Rao, Phys. Rev. B **66**, 064425 (2002).
[60] T. Shishidou, N. Mikamo, Y. Uratani, F. Ishii, and T. Oguchi, J. Phys.: Condens. Matter **16**, S5677 (2004).
[61] R. Seshadri and N. A. Hill, Chem. Mater. **13**, 2892 (2001).
[62] S. A. Wolf, D. D. Awschalom, R. A. Buhrman, J. M. Daughton, S. von Molnár, M. L. Roukes, A. Y. Chtchelkanova, and D. M. Treger, Science **294**, 1488 (2001).
[63] N. A. Hill and K. M. Rabe, Phys. Rev. B **59**, 8759 (1999).
[64] C.-H. Yang, T. Y. Koo, S.-H. Lee, C. Song, K.-B. Lee, and Y. H. Jeong, EPL **74**, 348 (2006).
[65] S. V. Kiselev, R. P. Ozerov, and G. S. Zhdanov, Sov. Phys. Dokl. **7**, 742 (1963).
[66] F. Sugawara, S. Iida, Y. Syono, and S. Akimoto, J. Phys. Soc. Jpn. **20**, 1529 (1965).
[67] F. Sugawara, S. Iiida, Y. Syono, and S. Akimoto, J. Phys. Soc. Jpn. **25**, 1553 (1968).
[68] H. Chiba, T. Atou, and Y. Syono, J. Solid State Chem. **132**, 139 (1997).
[69] H. Faqir, H. Chiba, M. Kikuchi, Y. Syono, M. Mansori, P. Satre, and A. Sebaoun, J. Solid State Chem. **142**, 113 (1999).
[70] P. Baettig, C. Ederer, and N. A. Spaldin, Phys. Rev. B **72**, 214105 (2005).
[71] A. A. Belik, S. Iikubo, K. Kodama, N. Igawa, S. Shamoto, M. Maie, T. Nagai, Y. Matsui, S. Y. Stefanovich, B. I. Lazoryak, and E. Takayama-Muromachi, J. Am. Chem. Soc. **128**, 706 (2006).
[72] A. A. Belik, S. Iikubo, T. Yokosawa, K. Kodama, N. Igawa, S. Shamoto, M. Azuma, M. Takano, K. Kimoto, Y. Matsui, and E. Takayama-Muromachi, J. Am. Chem. Soc. **129**, 971 (2007).
[73] C.-H. Yang, T. Y. Koo, and Y. H. Jeong, J. Korean Phys. Soc. **55**, 80 (2009).
[74] J. Li, J. Wang, M. Wuttig, R. Ramesh, N. Wang, B. Ruette, A. P. Pyatakov, A. K. Zvezdin, and D. Viehland, Appl. Phys. Lett. **84**, 5261 (2004).
[75] Y.-H. Chu, M. P. Cruz, C.-H. Yang, L. W. Martin, P.-L. Yang, J.-X. Zhang, K. Lee, P. Yu, L.-Q. Chen, and R. Ramesh, Adv. Mater. **19**, 2662 (2007).
[76] J. Y. Son and Y.-H. Shin, Appl. Phys. Lett. **93**, 062902 (2008).
[77] A. Sharan, J. Lettieri, Y. Jia, W. Tian, X. Pan, D. G. Schlom, and V. Gopalan, Phys. Rev. B **69**, 214109 (2004).
[78] C. Ederer and N. A. Spaldin, Phys. Rev. B **71**, 060401(R) (2005).